# JAAS

Accepted Manuscript


This is an *Accepted Manuscript*, which has been through the Royal Society of Chemistry peer review process and has been accepted for publication.

*Accepted Manuscripts* are published online shortly after acceptance, before technical editing, formatting and proof reading. Using this free service, authors can make their results available to the community, in citable form, before we publish the edited article. We will replace this *Accepted Manuscript* with the edited and formatted *Advance Article* as soon as it is available.

You can find more information about *Accepted Manuscripts* in the Information for Authors.



ROYAL SOCIETY OF CHEMISTRY

www.rsc.org/jaas

Journal of Analytical Atomic Spectrometry

RSCPublishing

ARTICLE

# In-*situ* scanning micro-XRF analyses of gilded bronze figurines at the National Museum of Damascus

Cite this: DOI: 10.1039/x0xx00000x

Received 00th January 2012,
Accepted 00th January 2012

DOI: 10.1039/x0xx00000x

www.rsc.org/

V. Kantarelou[a], A. G. Karydas[a,b], D. Sokaras[a*], L. Mahfouz[c], A. Qurdab[c], M. Al-Saadi[c], M. Giannoulaki[d] and V. Argyropoulos[d]

Scanning micro-XRF analyses were applied in-*situ* at the National Museum of Damascus in Syria for an analytical study of three unique gilded bronze figurines. The figurines are dated back to the Late Bronze age (1400-1300 BC) and were discovered at the Ugarit archaeological site in Syria. The present work focuses on analytical methodologies exploiting the merits of scanning micro-XRF analyses to provide an integrated non-destructive characterization of constituent materials (gilded layer, bronze alloy) or naturally formed corrosion layers. In the case of the XRF analysis of ancient bronze alloys, a universal dependence of the Sn Kα to Lα characteristic lines intensity ratio is proposed as a function of the Sn concentration. This consists a simple analytical quantitative criterion to assess the suitability of the surface preservation state before proceeding with any XRF quantification analysis. The results of the present study demonstrate and highlight the potential of scanning micro-XRF to expand the analytical information obtained beyond the spatially resolved elemental composition, thus offering more insight into metallurgical techniques applied by the ancient craftsmen.

[a] Institute of Nuclear Physics, NCSR Demokritos, 15310, Athens, Greece.
[b] Nuclear Science and Instrumentation Laboratory, International Atomic Energy Agency (IAEA), IAEA Laboratories, A-2444, Seibersdorf, Austria.
[c] Ministry of Culture, Directorate General of Antiquities & Museums, Syria.
[d] Technical and Educational Institute of Athens (TEI), Department of Conservation of Antiquities and Works of Art, Ag. Spyridona, 12210 Athens, Greece.
[*] Current Affiliation: SLAC National Accelerator Laboratory, 2575 Sand Hill Road, MS 69, Menlo Park, CA 94025, USA.

## Introduction

The National Museum of Damascus contains internationally significant archaeological and historical collections and the most important finds on display originate from excavations throughout Syria. From the section of the museum that it is devoted to Ancient Syria (from the end of the fourth millennium BC to the end of the first millennium BC) three unique bronze gilded figurines that had never been analyzed before were studied with micro-XRF analyses. The figurines belong to the Late Bronze age (1400-1300 BC) and were discovered at the Ugarit site. These statues represent ancient Gods, the first one is a figure of the El God (museum number RS23) and the other two of the Baal God (museum numbers 3572 and RS06 respectively) (Fig. 1).


Figure 1a-c: The Figurine 1 (left, museum no. RS23) resembles to El God, principal God of Ugarit (height 13.5 cm). The figurine was originally a gilded bronze but nowadays many gold parts are missing and the exposed areas are covered by a thick green corrosion layer. The Figurines 2 (middle, museum no. 3572), 3 (right, museum no. RS06) resemble to weather God Baal and have a height of about 12.5cm. The figurines were also originally gilded bronze but nowadays only some gold parts are preserved in the head area. All figurines belong to the late Bronze Age (14th century BC).

The El God figurine (Fig.1a) has never been treated and it is covered by thick layers of green and black colored corrosion products. The other two gilded figurines (Figs 1b, 1c) were treated with benzotriazole (BTA) and were protected with a wax coating.

The present study aims to determine the elemental composition and thickness of the gilding layers, to investigate the nature of corrosion products formed on the surface of the bronze figurines and to explore analytical criteria that will ensure that XRF data obtained noninvasively from the surface of the bronze alloy can accurately reflect its bulk composition. During the in-*situ* campaign elemental analyses of the gilded bronze figurines were also carried out using a portable LIBS spectrometer [1, 2].

The analytical possibilities of in-*situ* XRF analyses have been exploited and described in numerous publications [3-5]. In-*situ* micro-XRF analyses, and in particular those performed in a scanning mode, are relatively scarcely reported in the bibliography [6, 7]. The microscopic and highly localized analysis (at the scale of 0.1mm or below) has the great benefit to offer quantitative analysis of decorative details on artefacts whereas a scanning mode can further reveal spatially resolved elemental associations enriching the analytical information on manufacturing techniques and surface corrosion products. Nonetheless, the micro-XRF analysis could produce misleading qualitative or quantitative information for specific metal alloys that exhibit micro-scale heterogeneity, when not employed properly. For example, it is very characteristic that the homogeneity for the Standard Reference Materials (SRM) BCR-691 copper alloys is ensured only for a beam spot size at the order of 5 mm due to their micro-scale heterogeneity [8].

In the case of archaeological copper alloys, in particular, natural patinas are formed due to various corrosion processes initiated by burial and other atmospheric environmental factors. Since patinas present a rather complex and heterogeneous structure, the localized micro-XRF analysis is the most appropriate technique to elucidate corrosion formation mechanisms and to help identify relevant products. Developing methods for assessing the degree of the original surface alteration is of a paramount analytical interest. For the particular case of Cu-Sn binary alloys L. Robiola et *al*., [9] has introduced a scaling factor to convert the Sn concentration measured on the "passive" surface to the one that represents the Sn average alloy composition. Satovic et *al*., [10] have examined the suitability of portable XRF for bulk analysis of low corroded binary Cu-Sn alloys (thickness of the corrosion layer up to 25μm) concluding that portable XRF can yield very accurate quantification results. In another portable XRF analysis of Cypriot bronzes of the early Iron Age [11] it was found in some tested artefacts that the deviation between the initially selected points for analysis and the freshly-cleaned areas (after mechanical removal of a thin ~1mm corrosion layer) is rather small, less than about ≤5%. Orfanou and Rehren [12] analyzed bronze alloys of the first half of the first millennium BC by portable XRF analysis using two different protocols (noninvasively on the intact surface and in a cleaned area by established conservation methods) and Electron Probe Micro-Analysis (EPMA) [12]. The authors concluded that phenomena of differential corrosion of copper or tin in ancient bronzes and preferential depletion of the main alloy components, i.e. copper and/or tin affect the quality of surface XRF results by providing (mostly) higher values for tin. Depending on which layer of the corroded surface is analyzed, either tin or copper can be significantly enriched.

The variation of Sn-Ka to Sn-La intensity between non-corroded and corroded areas has been proposed in previous studies [13, 14] that could provide a good indication about the preservation state of the bronze alloy surface. This criterion is systematically studied in the present work and it is utilized as a quantitative measure to guide the user in the selection of proper analyzed spots for the quantification of the figurines bronze base alloy.

## Archaeological background

The three bronze gilded figurines were found together, in a southern area of Ugarit. Ugarit is the ancient name of Canaanite city which is represented by the archaeological site of Ras Shamra, on Syria's Mediterranean coastline. The site was first excavated in 1929 by the French archaeologist Claude Schaeffer who proposed after many decades of research that the city served as a link between Near East and the Aegean world. The site is still being excavated by a joint French and Syrian group and continues to produce information about the Late Bronze Age period of the Mediterranean [15]. At that period, Ugarit became the center of interaction between Egypt, Crete, Cyprus and Anatolia promoting the exchange of the first artistic styles within the ancient world. Ugarit art was influenced by the Egyptian art as observed in the examined artifacts. In the El God figurine (Fig. 1a), the existence of holes above the ears indicates that horns were once attached. The statue was designed in a seated position; its right hand looks to be waving or blessing a crowd, while the left hand seems that once it held a missing piece [16]**.** The El God appears to be fully dressed wearing sandals. The position of the other two statues indicates a warrior who is ready to strike (depicting most likely the Baal God, Figs 1b, 1c). Both statues depict a warrior with a head dressed with a high tiara and clothed in a short sarong while the feet are bare. The appearance of all figurines derives from Egyptian art and myths. The crown of El God resembles the crown of Osiris, and the stance of the second and third figurine (Baal Gods) is borrowed by the Egyptian images of triumphant kings striding over fallen enemies [17].

There are many papers that review the gilding procedures throughout antiquity [18-23]. Foil gilding was common in Mesopotamia with a mechanical or physical (pressed) application of a layer of gold onto the surface of a less precious metal. Gold foil is distinguished from gold leaf as having a thickness greater than 10 μm, while the gold leaf refers to a thickness smaller than 10 μm. According to Oddy [20] the ability to produce a thin gold leaf through the beating process became possible only when methods to purify gold became feasible in Mesopotamia around 2000 BC, since impurities in the gold did not allow for the production of a thin leaf. For the gilding application, the foil was wrapped and attached over edges and beaten using a hammer. By the first millennium BC grooves were cut into the base metal to secure the foil by hammering [21]. Once the gold leaf was invented, it was applied to many different types of materials (silver or copper alloy objects), either with an adhesive or through a process of burnishing into position (diffusion bonding with the base metal). However, burnishing of the gold leaf onto tinned bronzes is not possible because the diffusion of the tin results in embrittlement of the gold [21].

In the case of El God the gold covers the whole statue, but on the other two figurines the remaining gilded parts are found on the face-crown, which is rather unusual since in most of the

sculptures from Ugarit, the gold is applied only on the crown [16].

## Experimental

### The portable XRF spectrometers

For the scanning micro-XRF analyses a customized model of the ARTAX portable micro-XRF spectrometer was utilized (Bruker Nano GmbH). The spectrometer probe consists of an X-ray micro focus Rh-anode tube (spot size 50 μm x 50 μm, 50 kV (max), 0.6 mA, 30 W maximum power consumption with 0.2 mm Be window thickness) and a polycapillary X-ray lens as a focusing optical element (IfG) that offers a focal distance of about 21mm and a spatial resolution of about 40 μm (@ 17.4 keV) and 80 μm (@6.4 keV) when the unfiltered tube radiation is used as an exciting X-ray beam [14]. The X-ray detection chain consists of an thermo-electrically cooled 10 $mm^2$ silicon drift detector (X-Flash, 1000B) with FWHM equal to 146 eV (at MnKα and 10 kcps) coupled with a digital signal processor. A colour CCD camera attached to the spectrometer head can offer live documentary image of the analyzed spot, whereas together with a dimmable white LED for sample illumination and a laser beam indicator the reproducible positioning of the measuring probe with respect to the analyzed surface is guided. In Fig. 2, the probe of the micro-XRF spectrometer is shown during a measurement the bronze gilded figurine 1. The micro-XRF spectrometer head can perform measurements in a helium atmosphere that improves the detection of light elements; however, this option was not used during the in-*situ* measurements at Damascus museum due to logistic difficulties for the transportation of the pressurized He tank.

Figure 2: The head of the micro XRF spectrometer (ARTAX, Bruker Nano GmbH) during a measurement of the bronze figurine 1 at the Conservation laboratory of the National Archaeological museum of Damascus

Another portable XRF spectrometer with a spot size of about 3 mm in diameter has been also used in this study for calibration purposes during laboratory measurements. It is consisted of an Rh anode tube (max 50 kV, 50W maximum power consumption, Be window with 0.075 mm thickness), a Si-PIN detector (XR-100CR, Amptek Inc.) coupled with a digital signal processor (PX4, Amptek Inc.). Two lasers beams assist for the proper placement of the sample surface with respect to the reference plane [24].

### Materials and Methods

Nine (9) reference bronze samples provided from the Foundation of Research and Technology Hellas (F.O.R.T.H.), Institute of Electronic Structure and Laser (I.E.S.L.) were analyzed for calibration purposes using both the milli- and micro-XRF spectrometers. The Sn composition varied from 1-13% certified by ICP and EDXS analyses. For the micro-XRF analyses, a filtered and unfiltered excitation beam was utilized and an area of about 2x2$mm^2$ with 1mm step size was scanned for each sample (9 single measurements). Two experimental conditions were used with the milli-beam XRF spectrometer to optimize the excitation of Sn K and L lines; one at 40 kV operational voltage with the use of a composite filter and a second one at 15 kV, without the use of any filter [24].
Four reference gold alloys (www.fischer-technology.com ) with Au content varying from 58 to 95%, were used for calibration purposes of the micro-XRF spectrometer.

### Optimization of the micro-XRF measurements

The customized version of the Artax micro-XRF spectrometer used in this study was developed to optimize certain analytical features: a) an efficient dual detection of medium atomic number elements (e.g. Sn) through both the K and L series of characteristic X-ray lines and b) to allow increased versatility in the analysis of irregular surfaces. Both requirements can be fulfilled by selecting properly the polycapillary X-ray lens functional characteristics and the design of the probe geometry. At first, the selected polycapillary X-ray lens presented a gain factor [25, 26] for photons of energy close to 30 keV (capable to excite the K-lines of Sn) only three times less than the respective gain factor value for 3 keV photons. Thus, the detection limit (DL) for Sn in a bronze alloy was determined to be 0.01% and 0.02% using the Sn-Kα and Sn-Lα lines, respectively. These DLs were determined for a 100s measurement of the BCR-B standard bronze reference alloy (2.06 % Sn) operating the micro-XRF spectrometer without any filter at 50 kV and 600 μA. In addition, the focal distance of about 21 mm for the X-ray lens and the open geometry of the spectrometer head offer good versatility in analyzing curved surfaces (Fig. 2). Another optimization of the spectrometer set-up configuration was carried out in order to maximize the peak to background ratio in the analysis of relatively light elements (for example S, Cl, etc.) contained in a Cu alloy. In this case, the background below their characteristic X-ray peaks is mainly due to the incomplete charge collection (ICC) of the high intensity Cu K peaks; by adjusting properly the position of the X-ray detector and its integrated diaphragm with respect to the analyzed sample surface, the irradiated area of the detector crystal is restricted and the Cu-ICC contribution in the spectral background is reduced.
For the micro-XRF analysis of metal alloys an appropriate stratified filter had to be inserted in the exciting beam path, between the X-ray source and the sample. The filter eliminates the presence of diffraction peaks which might interfere with characteristic X-rays of analyzed elements, whereas it further improves the peak to background in the analysis of contained trace (with a concentration below 0.1%). On the contrary, for the analysis of corrosion products, an unfiltered exciting beam is preferred so as to attain an optimum analytical range for major-minor elements, whereas in this case the detection of trace elements is not so important. All areas were examined by single spot, line and area scans using filtered and unfiltered excitation beam. The filters that were used are a sandwich of the following foils Co (17.7 ± 1.3) μm, Ti (23.64 ± 0.18) μm and Pd (11.3 ± 0.3) μm, however, for the analysis of gold alloys only Ti and Co foils were used. In all measurements, the tube voltage and the current was set at 50 kV and 600 μA respectively. In the single spot analysis, the time of the measurement was 100s and on the area scans the time was set equal to 20s per step.
The quantification procedure was carried out by means of an in-house developed software based on the fundamental parameters

approach. To determine the X-ray lens transmission efficiency and instrumental geometrical factor a set of pure single element or compound targets were used. The quantification model developed was tested during an inter-comparison exercise organized by the Getty museum [27]. Four (4) reference bronze samples, labeled as I, J, K, L were measured at three (3) different areas using both the micro- and milli- beam XRF spectrometers. The relative percentage differences of the mean values of the determined concentrations from the certified values are presented in Figure 3. In some cases, the difference of the calculated values from the nominal ones is over 10%, this can be attributed to their low concentration in the sample.

(a)

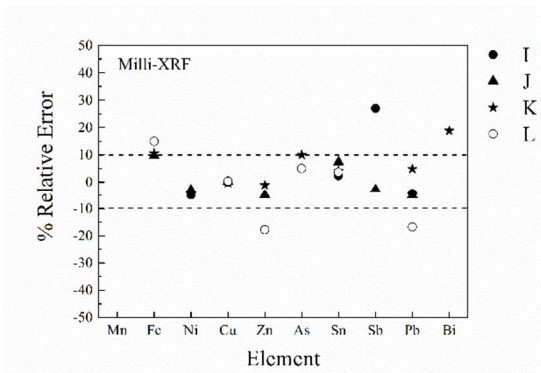


(b)

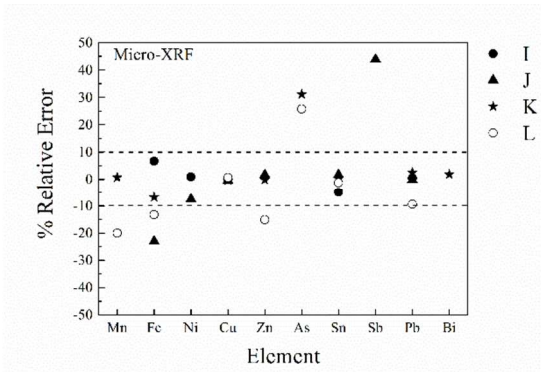


Figures 3a, b: The quantitative XRF model was validated using a set of bronze reference samples [27]. Every sample (labeled as I, J, K, L) was measured at three different areas using both a milli and micro XRF spectrometer. The obtained relative percentage differences of the mean concentration values with respect to the certified ones are displayed in Figs (a) and (b), respectively.

**A generalized quantitative XRF criterion to identify corroded areas in binary Cu-Sn alloys**

When XRF analysis is performed on bronze alloys, both Sn K- and L- shells can be efficiently ionized, when the tube high voltage is adequately above the Sn K absorption edge (in the range 40-50 kV). Consider a corroded bronze alloy that its near surface region is characterized by a heterogeneous structure with both the constituent Cu and Sn elements presenting an in depth variation of their abundance. In this case, it is expected that the intensity of L x-ray lines, due to their significantly lower energy than the K lines, would be more affected on the particular features of the formed surface stratigraphy. Below is an examination and validation of how the XRF (K/L) intensity ratio could be used as a rather sensitive quantitative criterion to identify corroded areas on bronze alloy surfaces:

The primary intensity $I_{p,i}(E_j)$ of an element $i$ characteristic X-rays with energy $E_j$ can be described by the fundamental parameter approach (FPA) in XRF analysis as follows:

$$I_{p,i}(E_j)=\frac{\Omega_d}{4\pi\sin\vartheta_1}\cdot\varepsilon_{ij}\cdot c_i\cdot\int_{U_{ij}}^{E_O}\frac{I(E)\tau_i(E)}{\mu_s(E,E_j)}dE=\frac{\Omega_d}{4\pi\sin\vartheta_1}\cdot\varepsilon_{ij}\cdot c_i\cdot\frac{1}{\mu_s(\overline{E}_j^S)}\int_{U_{ij}}^{E_O}I(E)\tau_i(E)dE$$

Where $\overline{E}_j^S$ denotes a mean energy that according to the first mean value theorem for integration fulfills the following relationship:

$$\frac{1}{\mu_s(\overline{E},E_j)}\int_{U_{ij}}^{E_O}I(E)\tau_i(E)dE\equiv\int_{U_{ij}}^{E_O}\frac{I(E)\tau_i(E)}{\mu_s(E,E_j)}dE$$

here $\Omega_d$ represents the solid angle of detection, $\varepsilon_{ij}$ the excitation factor of element $i$ characteristic X-rays with energy $E_j$, $c_i$ is the concentration of $i$ element in the sample, $U_{ij}$ and $E_o$ represent the $j$ absorption edge of element $i$ and maximum energy of the X-ray tube continuum radiation, respectively, $I(E)$ is the X-ray tube intensity, $\tau_i(E)$ is the photoelectric cross section of energy $E$ for element $i$,

$$\mu_s(E,E_j)=\mu_s(E)/\sin\vartheta_1+\mu_s(E_j)/\sin\vartheta_2$$

where $\mu_s(E)$ represents the total sample mass absorption coefficient for energy $E$ and $\vartheta_1$, $\vartheta_2$ are the angles that the exciting/fluorescence X-ray beams form with the sample surface.

In the case of the XRF intensity of Sn L lines emitted from a binary Cu-Sn alloy, the calculation is rather complex since various secondary enhancement effects contribute to their intensity: 1) the secondary fluorescence enhancement of Cu K lines to Sn L lines and the self-element one of Sn K to L lines [28], 2) the cascade K to L effect [29] and 3) the contribution of K, L photoelectrons and K- shell Auger electrons produced due to the ionization of Cu and Sn elements. These contributions can be summarized as $SE_{fl}, SE_{CE}$ and $SE_{el}$, respectively. Thus, the total XRF intensity of Sn Lα line can be written as follows:

$$I_{Sn}(L_\alpha)=I_{p,Sn}(L_\alpha)\cdot(1+\mathrm{SE}_{\mathrm{fl}}+\mathrm{SE}_{\mathrm{CE}}+\mathrm{SE}_{\mathrm{el}})\equiv I_{p,Sn}(L_\alpha)\cdot(1+SE_T)$$

The ratio of the XRF intensities Sn-Kα/Sn-Lα from an analyzed sample (denoted as S) to the respective ones obtained from the analysis of a Sn reference target (denoted as R, for example a binary Cu- Sn target with 10% content of Sn) can be written by combining the previous equations as follows:

$$G_{Sn}=\frac{\left(I_{Sn}(K_\alpha)/I_{Sn}(L_\alpha)\right)_S}{\left(I_{Sn}(K_\alpha)/I_{Sn}(L_\alpha)\right)_R}=\frac{\mu_R(E_1,E_{K\alpha})}{\mu_s(E_2,E_{K\alpha})}\times\frac{\mu_S(E_3,E_{L\alpha})}{\mu_R(E_4,E_{L\alpha})}\times\frac{(1+SE_T)_R}{(1+SE_T)_S}$$

Where the energies $E_i$ $(i=1,4)$ represent mean respective energies for the excitation of Sn-Kα and Sn-Lα characteristic X-ray lines, respectively. At first approximation and depending on the choice of the reference target (i.e. how it closely resembles the composition of the analysed samples), $E_1\approx E_2$ and $E_3\approx E_4$ so that each of the first two factors should be close to unity. The third factor, the only enhancement factor that

depends directly on the Cu concentration $(c_{Cu} = 1 - c_{Sn})$, expresses the secondary fluorescence enhancement of Cu-K lines to the Sn-L one; however, this contribution is estimated to be rather small compared to the rest of the secondary contributions which are, expected to be equal between the R and S targets. In conclusion, for a certain range of Sn concentrations in the binary Cu-Sn alloy system, the factor $G_{Sn}$ is expected to be rather constant and close to unity, although some weak dependence might be observed depending on the particular experimental conditions utilized for the excitation of Sn-Kα and Sn-Lα characteristic X-rays. On the contrary, in the case of a stratigraphic structure, any gradient in the depth distribution of Sn or Cu would affect critically its value due to the significant different self-attenuation of Sn-Kα and Sn-Lα characteristic X-rays in the alloy matrix.

The factor $G_{Sn}$ was determined using the set of bronze reference alloys mentioned above, and two different XRF spectrometers by applying three different excitation conditions: a) micro-XRF analysis with an unfiltered exciting beam (with 50 kV as an operational voltage), b) micro-XRF analysis with a filtered exciting beam (50 kV) and c) milli-XRF analysis using a filtered (40 kV) exciting radiation for Sn-Kα analysis and an unfiltered one (15 kV) for Sn-Lα analysis. The results are presented in Fig. 4. It can be observed that the factor $G_{Sn}$ varies for non-corroded bronze binary alloys within the range of values (0.89, 1.17) for Sn concentrations between 0 - 14%. According to the type of corrosion products which may be formed on the surface of a bronze binary alloy, the factor $G_{Sn}$ is expected to receive values below 0.89, if a Sn rich compound is formed on the alloy surface. On the other hand, in the presence of a Cu rich corrosion product, a value much higher than 1.17 is expected for the factor $G_{Sn}$, under the condition of course that the detection of Sn-Lα X-rays is still possible.

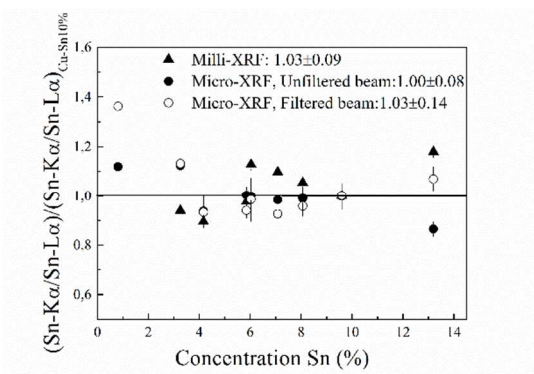


Figure 4: The variation of the Sn Kα/Lα normalized ratio (with respect to the value obtained from a binary Cu90% - Sn10% alloy), as a function of the Sn concentration measured from a set of reference binary Cu-Sn bronze alloys. The measurements were performed using two portable XRF spectrometers and three different experimental conditions.

## Results and discussion

### Gilding layer

The micro-XRF analysis of the gilded parts of the objects aimed to determine the thickness and composition of the gold foils and elucidate the technique of their application. For the determination of the gold foil thickness, the ratio of the Ag-Kα to Ag-Lα micro-XRF intensities [30] was measured with an unfiltered exciting beam from different gilded areas of the three figurines. The results obtained either from single spot measurements or from area scans represented by the mean value and standard deviation are presented in Fig. 5 together with respective values obtained from the set of available gold reference alloys. The theoretical dependence of the Ag-Kα/Ag-Lα ratio versus thickness shows an increase up to about 20 μm and then it saturates to a constant value. This dependence was calculated theoretically based on fundamental parameter approach for a typical Au alloy composition concentration (Au: 90%, Cu: 5%, Ag: 5%) and the obtained data was normalized to the experimental ratio deduced from a reference alloy of similar composition (Fig. 5).

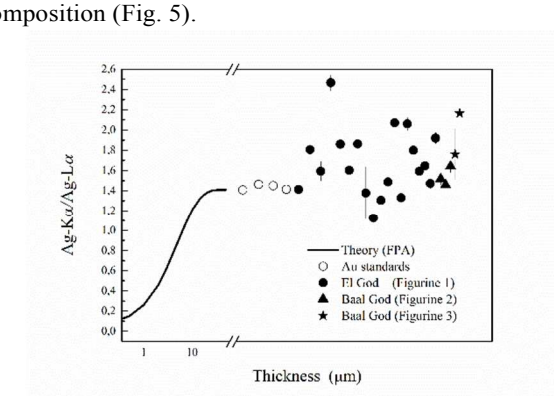


Figure 5: The dependence of the ratio Ag-Kα/Ag-Lα versus thickness was estimated theoretically for a typical Au alloy composition. The theoretical values are placed together with the intensity ratios measured from different gilded areas of the three figurines as well as with the ratios measured from reference gold alloys.

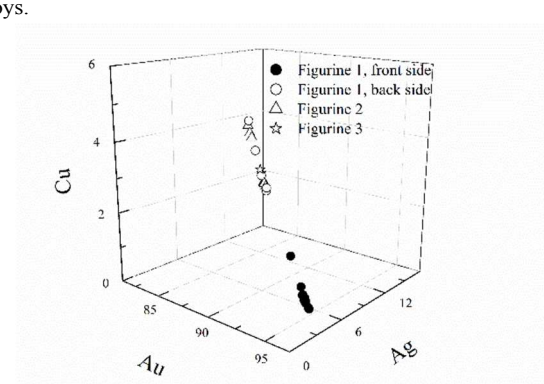


Figure 6: The 3D graph represents the Au, Cu and Ag concentrations of the gold foils used for the gilding of the three figurines. It is evident that the gold foils used for the figurine 1 (back side), figurine 2 and figurine 3 have similar composition, whereas in the front side of the figurine 1 the concentrations are different with the foil being significantly enriched in gold.

The measured Ag-Kα to Ag-Lα intensity ratios indicate that the gilding was applied with the use of a foil thicker than 10 μm. Such a foil thickness can be considered as a thick target for the quantification of the XRF intensities.

Journal of Analytical Atomic Spectrometry

RSCPublishing

ARTICLE

| El God_RS23, Micro-XRF analysis of gilded parts | | | | | | | |
|---|---|---|---|---|---|---|---|
| Photo of the area | | | File/ Description of the area | Filter/Number of measurements/ Time per step (s) /Area ($mm^2$)/Step (mm) | Concentrations ( wt % ) ( standard deviation in % of the characteristic X-ray intensities during area scans ) | | |
| | | | | | Au | Ag | Cu |
| 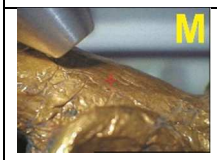 |  |  | M/ Head, crown, right side | No / 1/ 100 | 95.1 | 4.45 | 0.473 |
| | | | L / Head, crown, left side | No / 1/ 100 | 94.6 | 4.80 | 0.545 |
| | | | K / Head, right cheek | No / 1/ 100 | 95.1 | 4.25 | 0.587 |
|  | 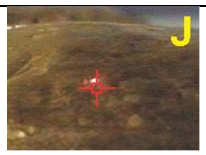 | 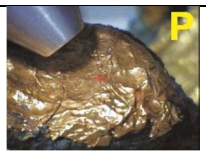 | I/ Head, crown, left side | No / 25 / 20 / 1 x 1 / 0.2 | 96.1 ± 0.3 (3.8) | 3.36 ± 0.27 (9) | 0.526 ± 0.050 (35) |
| | | | J / Head, crown, back side | No / 30 / 20 / 1 x 1 / 0.2 | 96.0 ± 0.5 (8.5) | 3.49 ± 0.51 (12) | 0.512 ± 0.061 (9) |
| | | | P / Hand, right | No / 1/ 100 | 94.6 | 4.55 | 0.797 |
|  |  | 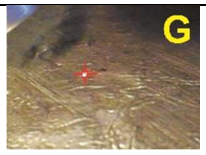 | U / Hand, left | No / 1/ 100 | 91.0 | 8.24 | 0.866 |
| | | | T / Arm, right | No / 1/ 100 | 94.9 | 4.57 | 0.510 |
| | | | G / Legs | No / 81 / 15 / 2 x 2 / 0.25 | 95.9 ± 0.8 ( 3.8 ) | 3.60 ± 0.76 ( 18 ) | 0.508 ± 0.115 ( 35 ) |
| | | | | Yes / 25 / 15 / 2 x 2 / 0.4 | 94.7 ± 0.3 (4.5) | 4.84 ± 0.33 (10) | 0.397 ± 0.050 (15) |
| 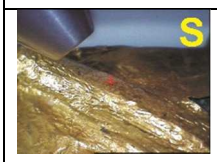 |  | 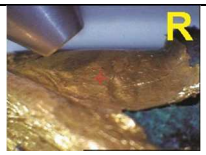 | S / Legs | No / 1/ 100 | 94.9 | 4.58 | 0.465 |
| | | | Q / Legs | No / 1/ 100 | 94.9 | 4.59 | 0.530 |
| | | | R / Legs | No / 1/ 100 | 95.1 | 4.44 | 0.413 |
|  | 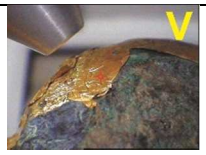 |  | X / Legs | Yes / 12 / 30 / 0.3 x 0.3 / 0.1 | 94.3 ± 0.3 (4) | 5.17 ± 0.34 (9) | 0.457 ± 0.050 (11) |
| | | | V / Back, right side | No / 1/ 100 | 83.2 | 14.5 | 2.18 |
| | | | W / Back, right side | No / 1/ 100 | 85.1 | 12.8 | 2.05 |
|  |  |  | F / Back, left side | No / 36 / 15 / 1.25 x 1.25 / 0.25 | 83.7 ± 2.4 (5.4) | 12.2 ± 1.4 (19) | 4.08 ± 1.95 (85) |
| | | | O / Back, left side | No / 1/ 100 | 83.9 | 14.3 | 1.75 |
| | | | N / Back, left side | No / 1/ 100 | 83.0 | 13.9 | 3.02 |

Table 1: Quantitative results from the Micro-XRF analysis of the different gilded parts of the figurine 1.The concentrations were measured either from single spot measurements or from the sum spectra resulted from area/line scans. In the latter case, the relative standard deviation (%) of the measured elemental intensities is reported in parenthesis, as deduced from all line/scan measurements. Individual photos of all analyzed areas are also shown together with the applied experimental parameters for each type of measurement.

| Baal God _RS06, Micro-XRF analysis of gilded parts | | | | | |
|---|---|---|---|---|---|
| **Photo of the area** | **File/ Description of the area** | **Filter/Number of measurements/ Time per step (s) /Area ($mm^2$)/Step (mm)** | **Concentrations ( wt % ) ( standard deviation in % of the characteristic X-ray intensities during area scans )** | | |
| | | | **Au** | **Ag** | **Cu** |
|  | A / Head, right cheek | No / 9 / 30 / 0.4 x 0.4 / 0.2 | 83.5 ± 0.4 (2) | 14.5 ± 0.4 (3) | 1.94 ± 0.18 (10) |
| | | Yes / 9 / 30 / 0.4 x 0.4 / 0.2 | 82.7 ± 0.5 ( 2 ) | 15.5 ± 0.5 (3) | 1.84 ± 0.18 (12) |
|  | B / Head, crown | No / 12 / 30 / 0.6 x 0.4 / 0.2 | 83.9 ± 0.8 (4) | 14.2 ± 0.5 (6) | 1.89 ± 0.64 (37) |
| | | Yes / 12 / 30 / 0.6 x 0.4 / 0.2 | 82.7 ± 0.7 (5) | 15.4 ± 05 (6) | 1.85 ± 0.51 (36) |
| 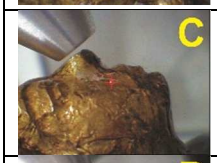 | C / Head, left cheek | Yes / 1 / 100 | 81.3 ± 0.1 | 15.0 ± 0.1 | 3.65 ± 0.03 |
|  | D / Head, back | No / 9 / 30 / 0.4 x 0.4 / 0.2 | 82.6 ± 1.4 (28) | 13.9 ± 1.0 (33) | 3.41 ± 0.95 (39) |
| | | Yes / 9 / 30/ 0.4 x 0.4 / 0.2 | 81.4 ± 1.7 (12) | 15.1 ± 1.3 (13) | 3.42 ± 1.08 (39) |
| **Baal God_3572** | | | | | |
|  | A / Head, right cheek | No / 12 / 30 / 0.4 x 0.4 / 0.1 | 83.3 ± 1.3 (33) | 14.2 ± 1.1 (37) | 2.41 ± 0.66 (31) |
| | | Yes / 12 / 30 / 0.4 x 0.4 / 0.1 | 82.7 ± 0.7 (33) | 15.1 ± 0.5 (32) | 2.19 ± 0.55 (36) |

Table 2: Quantitative results from the Micro-XRF analysis of the different gilded parts of the figurines 2 and 3.The concentrations were measured either from single spot measurements or from the sum spectra resulted from area/line scans. In the latter case, the relative standard deviation (%) of the measured elemental intensities is reported in parenthesis, as deduced from all line/scan measurements. Individual photos of all analyzed areas are also shown together with the applied experimental parameters for each type of measurement.

It is also interesting to note from Fig. 5 that the measured Ag Kα to Lα intensity ratios generally take a much higher value than around 1.4, that represents the saturation value experimentally deduced from the reference thick gold alloys.
In Tables 1 and 2, the elemental concentrations of the analysed gilded parts from the three figurines are presented. The results show that gold foils of different composition have been used to cover the front and back side of the first figurine, whereas the compositional profile of the gold foils applied in the other two figurines is very similar to the one used in the back side of the first figurine (Fig. 6). More specifically, the gold alloy used to cover the front side of the first figurine is of higher purity since the mean values (wt %) of all areas are for Au: 94.8 ± 1.1, Ag: 4.6 ± 1.1 and Cu: 0.52 ± 0.13, whereas the respective mean values for the back side are: Au: 83.4 ± 0.4, Ag: 13.6 ± 0.9 and Cu: 2.5 ± 0.9. In all area scans performed on the first figurine, the Cu concentration exhibits large variability. As an example, Figs. 7a-c show the spatial variation of the Au, Ag and Cu characteristic X-ray intensities obtained from an area scan performed on a gilded part of the first figurine (see Table 1, area analysed F).

(a)

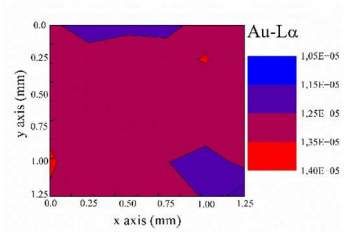


(b)

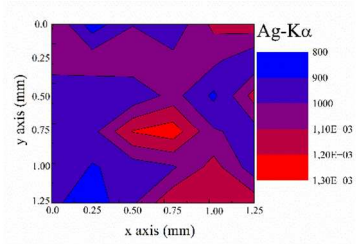

(c)

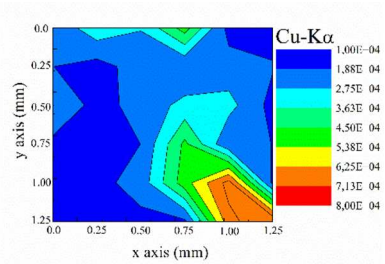


Figures 7a-c: Spatial distribution of Au, Ag and Cu, as determined from the micro-XRF scanning measurements of Au-Lα (7a), Ag-Kα (7b) and Cu-Kα (7c) characteristic X-ray intensities. The scanned gilded area is of 1.25 x 1.25 $mm^2$ and 36 measurements were performed with a step size of 0.25 mm from the back side (area 1F) of the first figurine

It can be observed that although Au and Ag are rather homogenously distributed, the Cu content shows generally large variation, especially in a localized region (in the right down corner) of the map area of Fig. 7, where Au shows also a 20|% relative decrease.

The technique applied for the attachment of the gold foils onto the surface of the statues was simple based on the ductility of the gold alloy [31]. The foils could be pressed onto the objects using processes such as hammering or pressed over the edges or in grooves of the objects [32]. There are no visible grooves on the examined objects, suggesting that the foils were mechanically fastened through the hammering process [19] and possibly by crimping [33]. The use of different gold sheets has been reported in [34] where it is noted that the Au content of the alloy used by the goldsmiths had very little, if any, importance at all. There have been studies [19, 20, 22] that report the technique of inserting a mineral layer, often called "white preparation" made of calcite or plaster (gypsum) between the substrate and the gold leaf. It is not well known if this layer contained additionally an organic binder [19]. However, there are no studies that report the use of such binding medium to the application of gold foil with thickness more than 10 micrometers and/or during the time period when the figurines were made. Without further scientific analysis underneath the gilded surface of the bronze figurines, it is difficult to investigate if any type of an organic binder still exists or was used. Another gilding technique, the so-called diffusion bonding technique [35] has been being employed at least as early as c.1200 BC, however it has been utilized for gold leafs and for not foils, whereas it is considered as more efficient method for the gilding of pure Cu and Ag alloys.

From the results of the micro-XRF measurements it is interesting to examine in more detail the relatively enhanced Ag Kα/Lα intensity ratio (see Fig. 5), as well as the increased variability of Cu-Kα intensity during area scans (see Tables 1-3, Fig. 7c).

For the first case, a reasonable explanation is that the Ag-Lα intensity is possibly affected from geometrical effects (foil roughness) or/and the presence onto the surface of a superficial corrosion layer. Both factors may result to a relative decrease of the Ag-Lα intensity. This is further supported by the fact that the observed variability of the Ag K/L intensity ratio mainly originates from the corresponding one of the low energy Ag-Lα characteristic X-ray lines.

The superficial corrosion layer could also explain the Cu spatial variability. Based on the calibration of the elemental response of micro-XRF spectrometer and with respect to the Cu spatial distribution as observed in Fig. 7c, it can be roughly estimated that a superficial Cu rich layer with about 150 nm thickness would be adequate to explain the increased intensity from the "cyan" to the "red" colored areas.

The alteration of the Au foil surface could be the result of selective dissolution of less noble metals such as Cu during long periods of burial or even of a microstructural heterogeneity formed during the temperature and mechanical processing of the foil (for production or/and application onto the base alloy). Furthermore, it cannot be excluded the possibility that through fissures or micro-cracks the surface has been contaminated in localized areas by Cu corrosion that has emanated underneath and this is in particular possible to the gilded areas close to the exposed bronze alloy and its corroded surface.

Selwyn [33] summarizes the corrosion phenomena for gilded metal, when gold foil is mechanically attached to metal by crimping, etc., and it is not well bonded to the surface. In this case wherever there is an opening through the gold such as at a crimp, water can penetrate and cause corrosion of the underlying metal, where eventually the corrosion products formed can force off the gold. However, in our case it appears to be no breaks in the foil. In one related study of a gilded Egyptian figurine of Osiris [36], remnants of gilding was found and analyzed (23 μm thickness), the Cu content was found quite variable reaching a very high concentration equal to 15 wt%. As a possible explanation for this high content the author proposed that the Cu is diffused towards the surface from the metal substrate (i.e. bronze alloy). However, it should be noted that the foil gilding on this figurine was in very poor condition in comparison to the figurines in the present study. There have been also other studies that have examined the corrosion of a gold foil/leaf although we cannot find exact similarities to the present case of gilded figurines. For example, Xingling et *al.* [37] have recently demonstrated the corrosion of a very thin pure gold leaf (leaf thickness equal to 95 nm with 98 wt% Au content) after exposure to certain atmospheric conditions (eg. RH, $SO_2$, $NO_2$). In a more relevant study of a Late Bronze Age gilded copper nail, E. Figueiredo et *al*. [35] have observed that the purified gold foil of 5-8 μm thickness was covered by a thick Cu based corrosion layer, whereas its significant enrichment in Cu was attributed to the corrosion of the base metal, the diffusion bonding or in combination of these two factors.

In summary, we can conclude that the methodology of performing micro-XRF elemental mapping of the figurines gilded parts could provide an indirect assessment of their preservation state (condition). When the variability of the measured characteristic X-ray intensities is rather small (below 5% relatively) then this could be an indicator for a rather good condition of the Au leaf/foil.

**Corroded areas on the bronze alloys**

In micro-XRF analysis of a naturally formed patina or corrosion layer the identification of the constituent compounds relies on the spatially resolved detection and association of particular elements (matrix elements together with low atomic number elements like S or Cl), which are considered fingerprints of certain types of Cu based corrosion products. It should be stressed, however, that the XRF analysis cannot identify the crystalline or molecular type of a corrosion product, as XRD, XAS, or FTIR analysis can perform respectively. However, scanning micro-XRF analyses can reveal spatially resolved elemental associations compatible with particular corrosion products.

The exposed areas of the first El God figurine (i.e. the ones that the gold foil is not preserved anymore) are mostly covered by a green thick layer, whereas on the other two figurines (Baal Gods) the green areas are restricted in localized spots. Four different green areas were analysed on the El God and one area from each of the other two figurines. In all, the acquired XRF spectra the Sn-L lines were missing. Moreover, the absence of Cl and S characteristic X-ray lines combined with the strong appearance of Cu one (Fig. 8) strongly indicates that a copper rich compound with very light, non-detectable, elements has been formed on the green areas (i.e. copper carbonate, malachite).

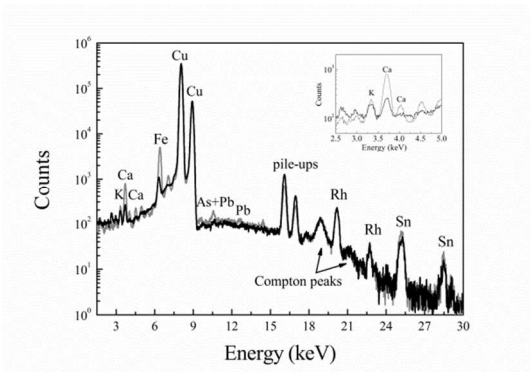


Figure 8: Representative spectra from two green areas of the exposed surface of figurine 1. The absence of S-K, Cl-K and Sn-L lines points to the formation of a Cu based corrosion product, possibly malachite (copper carbonate)

There are very few areas with the appearance of a black color, mostly on the Baal figurines. In the case of Figurine 1, a black area was exposed after removing locally with a mechanical means the green thick patina layer and area scan measurements were performed. In Fig. 9, the acquired single spot spectrum is presented. It is evident that due to the high intensity of Sn-L lines that most likely tin compounds, such as hydrated forms of Sn ($SnO_2nH_2O$) or stannic oxide ($SnO_2$) have been formed [38]. Single spot spectra from the black areas from the two Baal figurines are also shown in Fig. 9. In these two spectra the Sn-L lines are completely missing providing a strong indication that a thick patina layer rich in Cu oxides (possibly tenorite) is formed.

The reddish-brown areas appeared in the two Baal figurines most likely represent the closest to the original Cu alloy surface. In both Figurines, Cu and Sn were detected as major elements providing a strong indication that the Cu metal alloy used for the figurines is a binary Cu-Sn alloy. Micro-XRF single spot measurements were performed using an unfiltered and filtered exciting beam. The filtered exciting beam revealed the presence of Fe, Zn, As and Pb traces in the bronze alloy of both figurines, whereas in the case of the third figurine (Baal God RS06), Cr and Se traces were also detected (Fig. 10a). The unfiltered excitation showed strong presence of Sn-L lines (Fig. 10b).

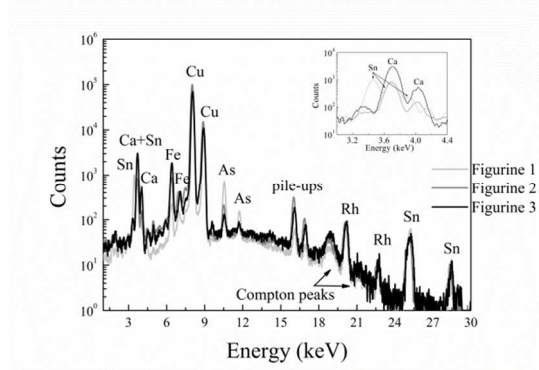


Figure 9: Single spot, spectra accumulated from black areas of the three objects whereas in the onset, a magnification in the region of Sn-L lines is displayed. In the case of El God (figurine 1), the presence of Sn-L lines is more intense pointing to the formation of Sn-rich compounds, whereas on the other two objects the reduction of these lines suggests the presence of Cu oxides (possibly cuprite).

(a)

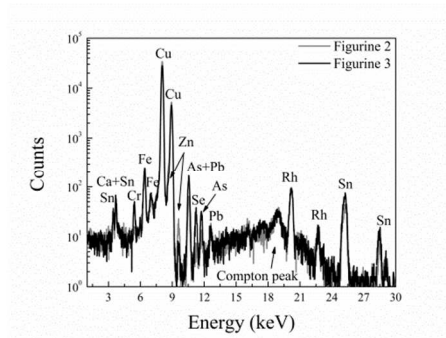


(b)

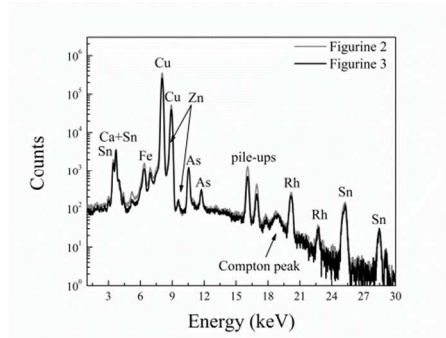


Figures 10a-b: Micro-XRF single spot spectra acquired from reddish-brown areas of the 2nd and 3rd figurine. (a) Filtered exciting beam: Cu and Sn are the major alloy elements in both figurines, Fe, Zn, As and Pb were detected in trace amounts, whereas in the 3rd figurine Cr and Se were also detected in traces (b) Micro-XRF analysis of the same spots as above but with an unfiltered exciting beam.

**Compositional analysis of the Bronze Alloy**

In order to identify suitable areas to apply quantification of the micro-XRF measurements performed on the three figurines, the $G_{Sn}$ criterion was utilized. The $G_{Sn}$ factors measured using an unfiltered exciting beam from brown-reddish and black areas of the three figurines are shown in Fig. 11.

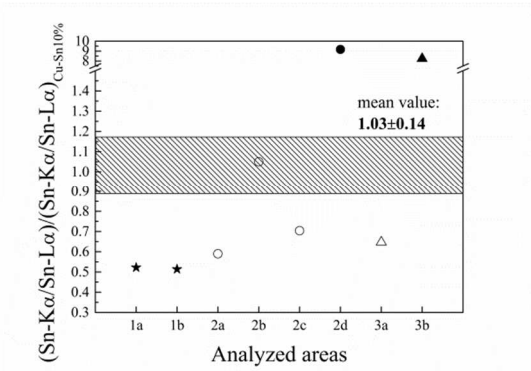


Figure 11: The $G_{Sn}$ values, namely the Sn Kα/Lα normalized ratio (with respect to a binary Cu90-Sn10 binary alloy), as obtained from micro-XRF measurements on brown-reddish (white spots in the graph) and black areas (black spots in the graph) of the three figurines. Only one value from a measurement on Figure 2 is within the "expected" range that corresponds to a corrosion free area appropriate for applying quantification of the micro-XRF data.

Only one measurement that corresponds to a brown colored area from figurine 2 is within the "expected" range of $G_{Sn}$ values ($G_{Sn}$ =1.05) indicating the presence a non-altered surface area of the binary Cu-Sn base alloy. For this particular spot the quantitative results are presented in table 3.

| Elemental composition of figurine 2 (wt %) | | | | | |
|---|---|---|---|---|---|
| **Fe** | **Cu** | **Zn** | **As** | **Sn** | **Pb** |
| 0.26 ± 0.03 | 92.5 ± 1.0 | 0.60 ± 0.06 | 0.10 ± 0.01 | 6.32 ± 0.30 | 0.040 ± 0.004 |

Table 3: Elemental composition of the base bronze metal for figurine 2. The quantification was performed for an analyzed spot were the $G_{Sn}$ factor was within the interval. The concentration values appear to be typical of the period and the area that were found.

The quantitative results for Baal figurine resemble typical concentrations of bronze alloys of the late Bronze period. The base alloy of the El God figurine seems to be also a binary Cu-Sn alloy with trace amounts of As. De Ryck et *al.* [39] suggested that during the Early Bronze Age copper arsenical alloys with an arsenic concentration up to 5% were generally applied and the introduction of tin bronzes was made during the middle of the 3rd millennium B.C. Rosenfeld et *al*. [40] studied 29 figurines and items of jewelry from the Middle Bronze Age that were originally found in Israel, Lebanon and Syria. In this study, the transition to tin-bronze during the Late Bronze Age is attributed to either the poisonous nature of As or the shortage in the supply of copper-arsenide ores. In 72% of the figurines that were analyzed, the Sn content was in the range of 7-15% with an average value of 6.4%. Furthermore, Braidwood, et *al.* [41] analyzed two bronze figurines from the beginning of the 3rd millennium BC and the tin concentration was found equal to 7.4% and 10.9 wt. % respectively.

## Conclusions

The results of a systematic micro-XRF analytical examination of three gilded bronze figurines at the National museum of Damascus were presented. The analytical study was carried out in-*situ* by means of a portable micro-XRF spectrometer and was based on various methodologies applied to exploit the analytical information and to minimize limitations raised from the non-invasive character of the investigation. The analysis of gilded areas provided information on the foil gilding technique, the elemental composition of the different gold sheets used on parts of the objects, and possibly the preservation state of the gilded areas. On the exposed areas of the three figurines, strong indications for the formation of various corrosion products (e.g. malachite, stannic oxide and copper oxides) were identified. For the case of the XRF analysis of an ancient bronze alloy, a universal quantitative criterion was proposed and validated allowing for proper assessment of the measured area suitability for noninvasive XRF quantification. Based on this criterion, the composition of the base alloy was determined for the Baal figurine 2 and was found to be a typical Cu-Sn binary alloy of the late Bronze period.

Overall, it was demonstrated the great potential of Micro-XRF portable instruments to provide advanced characterization of materials, in-*situ*. By developing careful and suitable methodologies for the instrument calibration and quantification procedure as well as criteria for assessing the suitability of the analyzed areas, ultimate analytical information can be obtained in-*situ* by combining the advantage of both the micro-size beam and the rastering capabilities of such instruments. In this present case, micro-XRF point analysis, of properly selected representative areas, offered reliable quantitation of decorative details on artefacts whereas the scanning mode revealed spatially resolved elemental associations indicating manufacturing techniques, surface corrosion products, and the condition of the objects. The general methodology and concept of approach presented here could be applicable to a broader range of in-field investigations.

## Acknowledgements

We would like to thank Mr Eythimios Bistekos for his technical assistance during the in-situ campaign in Damascus, Syria and Dr. Demetrios Anglos for providing the reference bronze samples. We are also grateful to Dr. Maamoun Abdulkarim, Mr Maher Azar, the staff of the Ministry of Culture of Syria and the curators of the National Museum of Damascus for providing the permission to study the unique gilded bronze figurines, for their hospitality and overall assistance during our campaign.

## Notes and references

†*PROMET EU-FP6 project (No. 509126, 2005-2008): Innovative conservation approaches for monitoring and protecting ancient and historic metals collections from the Mediterranean basin*

1 A.G. Karydas, D. Anglos and M.A. Harith, *Metals and Museums in the Mediterranean: Protecting, Preserving and Interpreting*, Ed. by V. Argyropoulos 2008.

2 Metals and Museums in the Mediterranean: Protecting, Preserving and Interpreting, Publications of the TEI of Athens, pp. 168-170, 2007.

3 *Portable X-Ray Fluorescence Spectrometry: Capabilities for In Situ Analysis*, Editors Phillips J Potts, Margaret West, Published by Royal Society of Chemistry, 2008.

4 G. Buzanich, P. Wobrauschek, C. Strelli, A. Markowicz, D. Wegrzynek, E. Chinea Cano, M. Grieserd and K. Uhlird, , *X-Ray Spectrometry*, 2010, **39**, 98–102.

5 Ch. Zarkadas and A.G. Karydas, *Spectrochemica Acta Part B*, **54**, 2004, 1611-1618.
6 K. Janssens, G. Vittiglio, A. Aerts, B. Vekemans, F. Wei, I. Deryck, O. Schalm, F. Adams, A. Rindby, A. Knöchel, A. Simionovici and A. Snigirev, *X-Ray Spectrometry*, 2000, **29**, 73–91.
7 K. Trentelman, M. Bouchard, M. Ganio, C. Namowicz, C. Schmidt Patterson and M. Walton, *X-Ray Spectrometry*, 2010, **39** 159-166.
8 C. Ingelbrecht, A. Andriaens, and E.A. Maler, The certification of arsenic, lead, tin and zinc (mass fractions) in five copper alloys, BCR-691, EUR 19778/1EN, 2001.
9 L. Robbiola, J. M. Blengino and C. Fiaud, *Corrosion Science*, 1998, **40**, 2083-2111.
10 D. Satovic, V. Desnica and S. Fasinic, *Spectrochimica Acta Part B*, 2013, **89**, 7-13.
11 A. Charalambous, V. Kassianidou and G. Papasavvas, *Journal of Archaeological Science*, 2014, **46**, 205-216.
12 V. Orfanou and T. Rehren, Archaeological *and Anthropological Sciences*, 2014, DOI 10.1007/s12520-0140198z.
13 A. Gianoncelli and G. Kourousias, *Applied Physics A*, 2007, **89**,857-863.
14 V. Kantarelou, A.G. Karydas, Ch. Zarkadas, M. Giannoulaki and V. Argyropoulos, *Proceedings of the International Conference on Conservation Strategies for Saving Indoor Metallic Collections (CSSIM)*, 2007, 93-99.
15 Beyond Babylon: Art, Trade and Diplomacy in the Second Millennium B.C. (Metropolitan Museum of Art), Edited by J. Aruz, K. Benzel and J. M. Evans
16 Marguerite Yon, The city of Ugarit at Tell Ras Shamra, Copyright 2006 by Eisenbrauns
17 Highlights of the National Museum of Damascus, Published by Meia Minds LLC, 2006.
18 P.R.S. Moorey, Ancient Mesopotamian materials and industries: the archaeological evidence, Oxford University Press, Oxford, 1999.
19 E. Darque-Cereti, E. Felder and M. Aucouturier, , *Revista Materia*, 2011,**16**, 540-559.
20 A. Oddy, *Cultural, technical& historical developments*, Susan La Niece, Paul Craddock, 1993, 171-181.
21 A. Oddy, *Gold Bulletin*, 1981, **14**,75-79.
22 A. Oddy, *Endeavour*, 1991, **15**, 29-33.
23 L. Selwyn, *Metals and Corrosion A Handbook for the Conservation Professional*, Canada 2004, 76-78.
24 A.G. Karydas, *Annali de Chimica*, **97**, 419–432.
25 N. Gao and I.Y. Ponomarev, *X Ray Spectrometry* 2003, **32**, 186-194.
26 J. Gormley, T. Jach, E. Steel and Qi-Fan Xian, *X Ray Spectrometry*, 1999, **28**, 115-120
27 A. Heginbotham, M. Bouchard, J.M. Davis, K. Eremin, J. H. Frantz, L. Glinsman, L. Hayek, D. Hook, V. Kantarelou, A. Karydas, L. Lee, A. Lins, J. Mass, C. Matsen, B. McCarthy, M. McCath, B. Price, A. Shugar, J. Sirois, D. Smith and R.J. Speakman, *Proceedings of the interim meeting of the ICOM-CC metal working group*, 2010, 244-255.
28 A.G. Karydas, *X-Ray Spectrometry*, **34**, 2005, 426-431.
29 D. Sokaras, A.G. Kochur, M. Kolbe, B. Beckhoff, M. Mantler, Ch. Zarkadas, M. Andrianis, A. Lagoyannis and A.G. Karydas, *Physical Review A*, 2011, **83**, 052511.
30 R. Cesareo and A. Brunetti, *Journal of X- Ray Science and Technology*, 2008, **16**, 119-130.
31 J. Altman, Gold Bull, Vol12, Issue2, pp75-82, 1979.
32 T. Ornan, Proceedings of the 7th International Congress on the Archaeology of the Ancient Near East, 2010, 2, 445-451.
33 L. Selwyn, Gilded Metals, History, Technology and Conservation, Ed. T. Drayman-Weisser, Archetype Publications, 2000, 21-48.
34 Archaeology After Interpretation: Returning Materials to Archaeological Theory, Edited by B. Alberti, A. Meirion Jones, J. Polland, ISBN-13: 978-1611323412, 2013.
35 E. Figueiredo, R. J. C. Silva, M. F. Araújo and J. C. Senna-Martinez, Microchimica Acta, 2010, 168, 283–291.
36 D. A. Scott and L. Swartz Dodd, Journal of Cultural Heritage, 2002, 3, 333–345.
37 T. Xingling, M. Qinglin, Z. Mingtian and L. Zhilin, *Rare Metal Materials and Engineering*, 2014, **43**, 2637-2642.
38 L. Robbiola and L.-P. Hurtel, *Proceedings of METAL 95: International conference on metals conservation*, 1995, 109-117.
39 I. De Ryck, A. Andriaens and F. Adams, *Journal of Cultural Heritage*, 2005, **6**, 261-268.
40 A. Rosenfeld, S. Ilani and M. Dvorachek, Journal of Archaeological Science, 1997, **24**, 857-864.
41 R. J. Braidwood, J. Burke and N.H. Nachtrieb, *Journal of Chemical Education*, 1951, **28**, 87-96.